Return maps for intensity and time in a homoclinic-chaos model applied to a laser with a saturable absorber

F. Papoff
Scuola Normale Superiore, Piazza dei Cavalieri 6, 56100 Pisa, Italy
and Dipartimento di Fisica dell'Università di Pisa, Piazza Torricelli 2, 56100 Pisa, Italy

A. Fioretti and E. Arimondo
Dipartimento di Fisica dell'Università di Pisa, Piazza Torricelli 2, 56100 Pisa, Italy
(Received 14 January 1991; revised manuscript received 22 April 1991)

Intensity maps from an experiment on a laser with a saturable absorber, in the case of strong dissipation, are compared with theoretical one-dimensional (1D) maps. These 1D maps are derived in the limit of infinite dissipation, starting from 2D maps for a dissipative saddle cycle with stable and unstable manifolds approaching a quadratic tangency and giving rise to a structurally unstable homoclinic orbit. They are multibranched, each branch corresponding to a particular number of turns around the saddle cycle. The good agreement between theory and experiment indicates that the origin of the complicated behavior of a laser with a saturable absorber is a saddle cycle. A multibranched structure is also present in maps of time of flight between planes in phase space. Depending on the choice of these planes, it is possible to obtain time-of-flight maps that give the same symbolic dynamics of the intensity maps.

PACS number(s): 42.50.Tj, 42.55.Em

I. INTRODUCTION

Homoclinic orbits have assumed great importance in the investigation of nonlinear-dynamical systems. These orbits are at the origin of chaotic behavior. Well known experimental evidence of the role played by homoclinic orbits has been provided by chaos in the Belousov-Zhabotinskii (BZ) reaction [1], in the feedback laser [2], and in the optically pumped far-infrared laser [3]. Observation of chaos in a laser with a saturable absorber (LSA) has also been associated with the presence of homoclinic orbits [4-7]. Until now experimental chaos in lasers was connected with systems having a homoclinic orbit associated with an equilibrium point of saddle type. The present investigation is concerned with another configuration, a tangent homoclinic orbit to a periodic motion, which is well known in dynamical theory for giving rise to chaotic behavior [8,9]. Thus we consider systems having a homoclinic orbit with a periodic motion of saddle type, and on which the stable and unstable manifold of the periodic solution are tangent so that the homoclinic orbit is structurally unstable. The homoclinic tangent bifurcation is itself embedded in an infinite set of bifurcations, typically saddle node and period doubling, and cannot be encountered as the initial change one sees for the birth of a strange attractor. Nonetheless it has been demonstrated by Gavrilov and Sil'nikov [8,9] that, with a particular geometrical configuration of the stable and unstable manifolds, it is possible, varying the control parameters, to start with a single global solution, and follow a sequence of bifurcations which lead to the development of increasingly complicated dynamics. Finally the control parameter allows the system to reach chaotic dynamics even if the stable and unstable manifolds have not yet had their first intersection. The relation between tangent homoclinic orbits and the mixed mode oscillation in the thermokinetics of hydrocarbon oxidation has been well established by Gaspard and Wang [10]. In quantum optics, Hammel, Jones and Moloney [11] have proven the influence of homoclinic tangency on the dynamics of a plane-wave intracavity field in ring resonators, while in the LSA that relation has been supported by a systematic numerical analysis [12].

Nonequilibrium behavior can be modeled by nonlinear systems involving a small number of variables. Thus one-dimensional (1D) or two dimensional (2D) return maps of the experimentally recorded variable and of the return time have been used to account for the chaotic dynamics. For instance, for the homoclinic chaos in the BZ reaction, 1D maps were used by Simoyi, Wolf, and Swinney [13] and Pikovsky [14], while 2D maps were used by Gaspard and Wang [10] to analyze the homoclinic orbits in the thermokinetics. Concerning LSA experiments, return maps of the laser intensity were initially derived by Tachikawa *et al.* [5]; later, laser intensity return maps have been used by Hennequin *et al.* [15] to show the analogy between LSA and BZ chaotic behavior. Return time maps have been introduced by Arecchi *et al.* [2] for the laser with electronic feedback to analyze homoclinic chaotic behavior. These maps are much easier to extract from experimental data because they do not require the reconstruction of the embedding space, which is usually a nontrivial problem. Return time maps for the LSA have been previously reported in Refs. [7] and [16].

The purpose of this paper is to derive 1D maps for systems approaching homoclinic tangency to a periodic motion in the hypothesis of infinite dissipation, and to use these maps in order to analyze intensity return maps and return maps for time of flight and return time recorded in LSA experiments. It is not the main purpose of this pa-

per to investigate the conditions for the occurrence of homoclinic tangency to a periodic motion in LSA as a function of the control parameter or the comparison with numerical results of LSA models. These topics are planned to be presented in a separate paper. Here we use the 1D maps to test for the periodic motion homoclinic tangency in LSA experimental data.

Another original and important result of the present paper is the derivation of the time return maps for systems approaching homoclinic tangency to a periodic motion. The hypotheses here applied to obtain time return maps are quite different from those applied in Ref. [2] for the case of a homoclinic orbit to a saddle focus. In the former the system spent most of the time around the saddle focus, in a region where the dynamics is determined by the linearization of the flow, while the time spent along the homoclinic curve was almost constant. In our case the time spent by the system in the region of phase space far from the periodic motion, during the reinjection process, directly provides important information on the dynamics. This behavior is illustrated by inspection of Fig. 1 where the region of phase space visited by the system during the reinjection process, the periodic motion L, and the section planes S_1 and S_2 are shown. The time of flight from S_1 to S_2 constitutes the time of the reinjection process measured by us. When the homoclinic curve to a saddle cycle exists, it turns an infinite number of times around the saddle cycle. Even if the time corresponding to the homoclinic orbit is infinite, the time corresponding to each single turn around the saddle cycle is bounded and could provide information on the chaotic dynamics. A result of this paper is that 1D maps may be used to identify systems in which stable and unstable manifolds of a structurally stable periodic solution of saddle type are approaching the tangency of the homoclinic bifurcation. When the tangency is realized, a structurally unstable homoclinic curve, i.e., a path biasymptotic to the periodic motion, is generated.

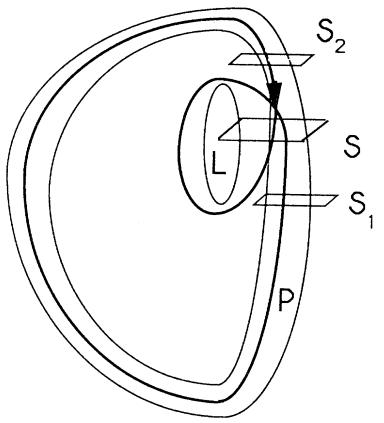

FIG. 1. Schematic representation of a periodic orbit P (heavy line), revolving around the saddle cycle L. The boundary of regions explored by the system during the reinjection process is sketched. The section planes S, S_1, and S_2 are used to investigate the orbits.

The 1D maps here presented may be used to reproduce most of the interesting features detected in chaotic systems with a homoclinic curve to a saddle cycle. The experiments we consider refer to strongly dissipative systems, so that the limiting case of infinite dissipation may be used as a rough approach to analyze the experimental results. We may ask which experimental features will be preserved in the simplified model of infinite dissipation and which features will be lost. It has been proven by Holmes and Whitley [17] that a decrease in dissipation may change the order of the different bifurcations but does not introduce any new orbit. Another feature of 2D maps, absent in the 1D case, is the presence of wild hyperbolic sets at the homoclinic tangency, as pointed out in Guckenheimer and Holms [18]. In the experiments we consider, the chaos is produced before reaching and far from the homoclinic tangency, so that the wild hyperbolic sets are not very important for our analysis. In most experiments, the dissipation is large enough to produce a sequency of appearance of stable periodic solutions equivalent to that of the 1D model. In particular, the 1D model explains and reproduces two main experimental features associated with an unstable homoclinic curve: (i) the chaotic signal appears as a mixture of a few stable solutions in regions of the control parameters space close to the chaotic region and (ii) the experimental return maps of either the intensity or the return times are multibranched. As a final important result of this paper the comparison between the LSA maps and those of a structurally unstable homoclinic curve confirms the interpretation that LSA is moving in a region along the homoclinic path formed by the stable and unstable manifolds of the saddle cycle.

Section II recalls the basic experimental setup for LSA, the basic observations of chaotic evolution, and the procedure adopted to analyze the recorded signals of the laser output intensity versus time. This material has been already presented by us in previous papers [4,7], so that the LSA review will be very sketchy. The connection between the LSA analysis and that applied for the BZ reaction by Argoul, Arneodo, and Richetti [19] will be pointed out. The key point for the comparison to the theoretical 1D maps is the derivation of the return maps for the laser intensity, and the return maps for the return time and time of flight, obtained from Poincaré sections of the phase-space reconstruction. In this paper we will present an analysis of LSA chaotic behavior using CH_3I as the saturable absorber, a molecular gas already investigated in Ref. [6]. An important part of the LSA analysis is the correlation between the observation of multibranched structured chaotic behavior and the spectroscopic parameters of the absorber. This point will be discussed in detail in a following paper [20]. In Sec. III the 2D maps reproducing the trajectories in phase space lying in the neighborhood of homoclinic curve are presented, and their reduction to 1D maps in the hypothesis of infinite dissipation is recalled. Section III deals also with the region of bistability and instability within the 1D maps. Section IV contains the derivation and application of return time maps. In Sec. V the return maps obtained from the 1D maps are compared to LSA experimental data.

Section III contains some very mathematical parts describing the analysis of the theoretical 1D maps and the associated maps of return times and times of flight. These mathematical parts are not required for a general comparison between 1D and LSA maps. Thus a preliminary reading of the paper may be restricted to Sec. III A.

II. LSA EXPERIMENTAL SETUP AND DATA

The measurements were made on a CO_2 laser operating on the $10P(32)$ line with the saturable absorber CH_3I gas in the presence of He buffer gas, in the 1:10 pressure ratio. The basic laser setup, essentially identical to that used in Ref. [7], is composed of an infrared cavity containing both the discharge CO_2 amplifier and an absorber cell. The I laser output intensity is recorded versus time as function of the laser control parameters. Stable LSA conditions were achieved by control of the discharge current. The experimental parameters are the discharge current, the absorber pressure, and the laser frequency detuning.

A short section of a typical time series is shown in Fig. 2(a), with a chaotic sequence of pulses defined as $P^{(0)}$ and $P^{(1)}$ in Ref. [7]. Recall that in the region of LSA instabilities and chaos the laser intensity pulse starts, from zero value, always with a large peak followed by a variable number of smaller peaks. Long-time series, up to 32 000 8-bit data, were stored in a microcomputer by use of a digital scope. Three-dimensional phase-space portraits were derived from the stored data, by plotting $I(t+2\tau)$ versus $I(t+\tau)$ and $I(t)$, where τ is a variable delay. Our space phase portrait is a three-dimensional projection of the attractor reconstructed through the time delay embedding. For different values of the delay time τ and for different viewing angles of the three-dimensional figure, one obtains some insight into the spatial structure of the attractor underlying the data set. Figure 2(b) shows the phase-space portrait reconstructed from the pulses reported in Fig. 2(a) through the time delay embedding. The underlying attractor of the chaos contains a well-determined hole, produced by the smaller pulses in the laser intensity, if the delay is of the order 1/20th of a period. For longer delays the attractor appears folded in a very strange manner with flat parts like wings of different orientation in phase space.

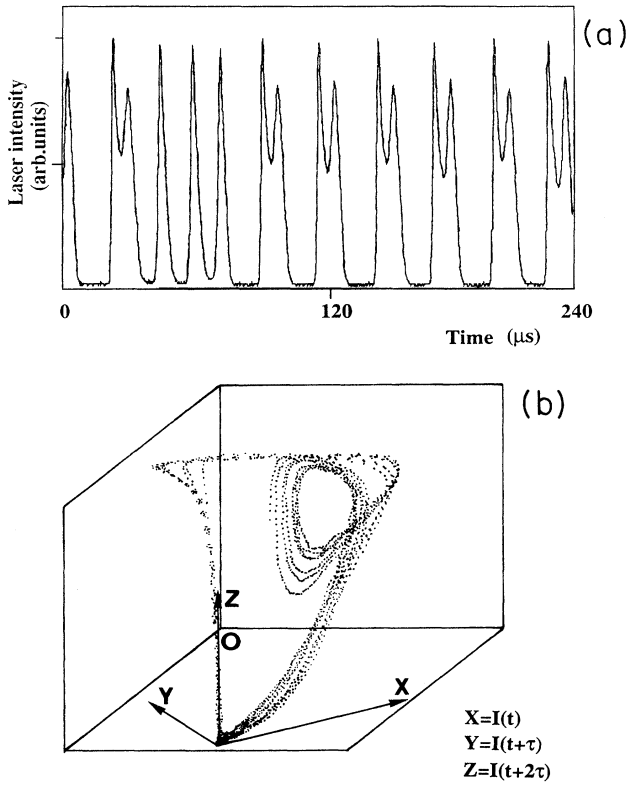

FIG. 2. In (a), sample of the laser output intensity I vs time t recorded on the LSA operating on the $10P(32)$ CO_2 laser line at 13.2-mA discharge, with saturable absorber CH_3I:He mixture 0.17 mbar total pressure in 1:10 ratio. In (b), corresponding 3000 point phase portrait in a three-dimensional space obtained with a time delay embedding. On the three axes $I(t)$, $I(t+\tau)$, and $I(t+2\tau)$, respectively, with $\tau=0.8$ μs.

The phase-space portrait of Fig. 2(b) and its comparison with Fig. 1 suggest that, when the small peaks in the laser intensity are observed, the system is moving in the neighborhood of a saddle cycle. Furthermore, when the laser intensity goes below the detection limit and increases again with a large peak, the system moves far from the saddle cycle and is then reinjected back into the saddle cycle.

In order to compare the experimental observations with maps, we use the technique applied successfully by Argoul, Arneodo, and Richetti [19] to analyze the BZ reaction. Once we have a 3D faithful phase-space reconstruction of the phase space, as in Fig. 2(b), we intersect the orbit in this space with a 2D plane conveniently chosen to be quasitransverse to the trajectories switching from one side to the other of the section. A 2D Poincaré map is obtained through that intersection. In the large majority of investigated cases the whole set of experimental points in the Poincaré map lie along a smooth curve that attests to the presence of a strong transverse packing associated with the presence of strong dissipation. If the points on the Poincaré section lie on a unidimensional manifold, we may define a coordinate system on the manifold and define a 1D return map by plotting the z_{i+1} coordinate versus the z_i coordinate, where the subscripts i and $i+1$ denote successive intersections with the 2D Poincaré plane. Application of this procedure to the data of Fig. 2 has produced the laser intensity return map of Fig. 3(a). Two branches are observed on that return map, and a closer inspection of the LSA data allows us to identify each branch with laser pulses having zero small pulses after the first large one ($n=0$), and laser pulses having one small pulse after the large one ($n=1$). This identification corresponds to orbits in the phase space with zero or one revolution along the saddle cycle, as in Figs. 1 and 2(a).

Concerning the return maps of time, let us notice first that in LSA the planes of Fig. 1 are defined by constant laser intensity. In effect the laser intensity is the observed

variable and one of the variables of the embedding space. Thus the times of flight between the S_1 and S_2 planes of Fig. 1 are obtained by defining two thresholds for the laser intensity and measuring in two consecutive pulses the times when, at the end of the ith pulse, the intensity goes below the first threshold to the instant, at the beginning of the $(i+1)$th pulse, where the intensity goes over the second threshold. In this way a time related only to the reinjection process is measured. This approach has been applied to derive from the records of Fig. 2 the data of Fig. 3(b), where maps of the time of flight are reported for the same experimental parameters used in Fig. 3(a).

In Figs. 3(a) and 3(b) two branches corresponding to $n=0$ and 1 are observed. As explained in the following, because the two maps have the same number of branches with the same slope, they are equivalent from the point of view of the symbolic dynamics [21]. In LSA, as well as in systems with homoclinic tangency to a saddle cycle, the time return maps give the same information as the Poincaré section laser intensity maps described previously, but with the enormous advantage that time return maps are much easier to be extracted from experimental data.

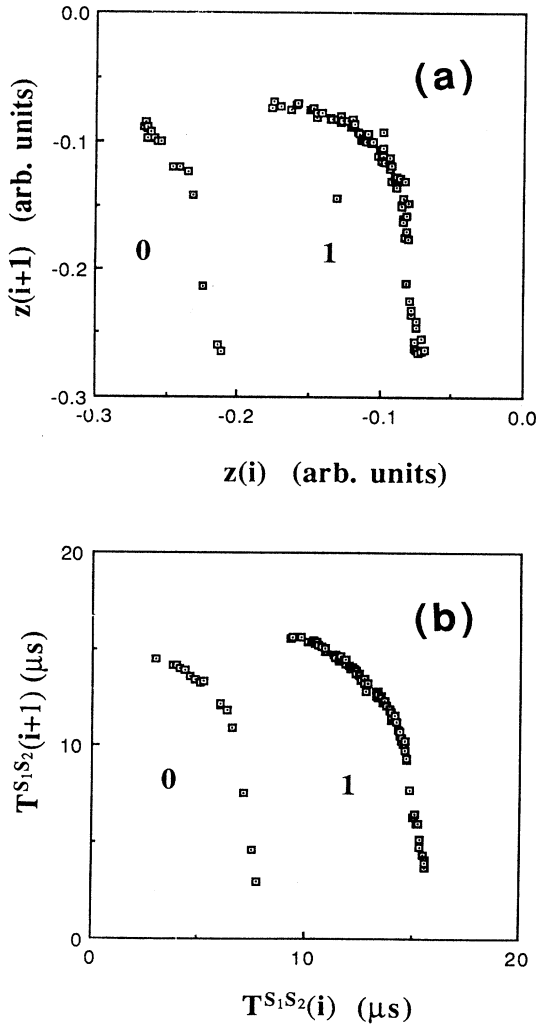

FIG. 3. Intensity return map, in (a), and time-of-flight T^{S_1,S_2} return map, in (b), from the records of Fig. 2. 102 data points, derived from the experimental recorded long-time series, are reported in the plots.

On an LSA experimental record similar to Fig. 2, except for the absorber pressure and the number of small peaks after the large pulse, we have also measured the return times between two consecutive interceptions on the plane S_1, i.e., the total time T^{ret} between the starting of the ith pulse and the starting of the next $(i+1)$th pulse. This time is related to both processes, the motion near the saddle cycle and the reinjection. The experimental results for the map of the return time T^{ret} are shown in Fig. 4(b), while Fig. 4(a) reports the times of flight, defined as the time required to have the laser evolving between two constant intensity planes in the region of zero laser intensity. In the experimental map of Fig. 4(a) we observe three different branches, corresponding to $n=0,1,2$. The return time return maps are composed of a greater number of branches than in the case of the time of flight.

III. 2D AND 1D MAPS

A. Global maps

Before studying the 1D maps, we give here a brief review of some mathematical results obtained with 2D maps in the hypothesis of a structurally unstable homoclinic orbit originated by a quadratic tangency between the stable and unstable manifolds of a saddle cycle [8,9].

Consider the one-parameter family of three coupled differential equations with control parameter μ

$$\frac{d\mathbf{X}}{dt}=\mathbf{G}_\mu(\mathbf{X}) , \tag{1a}$$

where $\mathbf{G}_\mu$ is C^k with $k\geq 3$, and we suppose these equations to have a periodic orbit of saddle type. The stable and unstable manifolds W^s, W^u of the saddle orbit are supposed to have a point of quadratic tangency along some homoclinic curve Γ doubly asymptotic to a periodic orbit L of Fig. 1 at $\mu=0$. As pointed out by Gavrilov and Sil'nikov [8,9], the study of the trajectories which lie entirely in small neighborhoods of the periodic saddle orbit and of its manifolds may be reduced to the study of a one-parameter family of maps of R^2 defined on Poincaré plane S transverse to the periodic orbit L (see Fig. 1).

On this plane we may use a reference frame whose origin is the intersection of the saddle cycle with the plane itself, and whose x and y axis coincide with the local stable and unstable manifolds. In this reference frame it is possible to reduce Eq. (1a) to the form

$$\begin{aligned}\frac{dx}{dt}&=Ax+\phi(x,y,\theta)x ,\\ \frac{dy}{dt}&=By+\gamma(x,y,\theta)y ,\\ \frac{d\theta}{dt}&=1 ,\end{aligned} \tag{1b}$$

where ϕ and γ vanish at $x=y=0$, and $A<0$, $B>0$ [22].

The global maps introduced by Gavrilov and Sil'nikov are constructed with the help of two maps T_0 and T_1. T_0 is used to mimic the motion near the saddle cycle and is a linear map, T_1 is used to imitate the reinjection process due to the motion near the unstable manifold and has a quadratic form due to the geometry of the unstable manifold. Maps T_1 and T_0 take the form

$$T_1(x,y)=(x_H+a(y-y_H),b\mu+cx+\tfrac{1}{2}d(y-y_H)^2)\ , \tag{2a}$$

$$T_0(x,y)=(\lambda_s x,\lambda_u y)\ , \tag{2b}$$

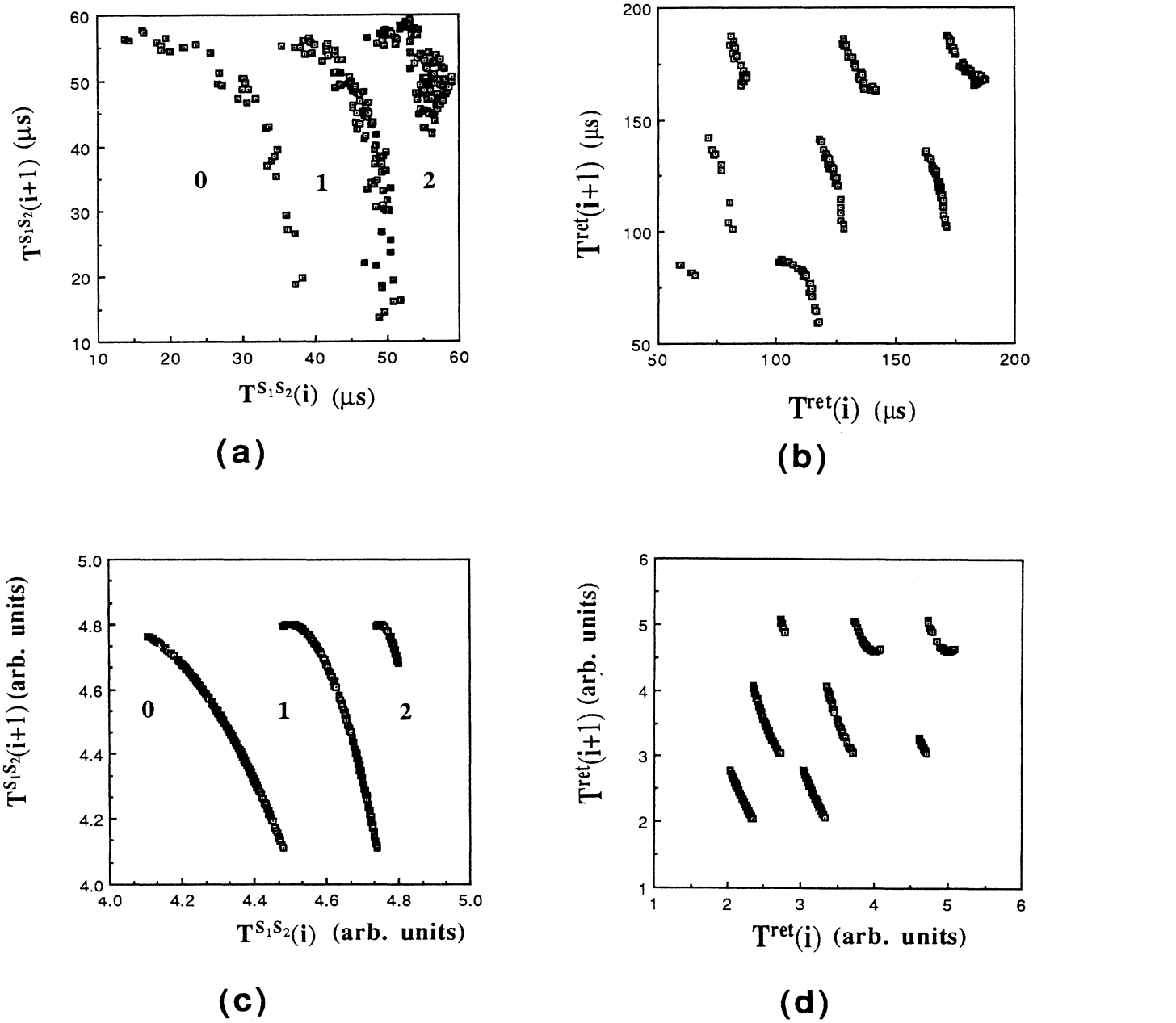

FIG. 4. In (a) time-of-flight T^{S_1,S_2} return map; in (b), return time return map as obtained from a LSA record with LSA operating on the 10P(32) CO_2 laser line at 10.8-mA discharge, with saturable absorber CH_3I:He mixture 0.10 mbar total pressure in 1:10 ratio, for 229 data points. In (c), theoretical time-of-flight T^{S_1,S_2} return map [Eq. (27)]; and (d) theoretical return time return map [Eq. (28)] obtained for the following control parameter values: $b=1$, $d=6$, $\lambda_u=2$, $\mu=0.18$, $\epsilon_1=0.48$, $\lambda_u^{-1}(1+\epsilon_2)=1-\epsilon_1$, $\alpha=T_C=T^*=1$.

where y_h is the vertical coordinate of the point which lies on the unstable manifold W^u and is mapped by T_1 into the point with minimum vertical coordinate, whose horizontal coordinate is x_H. Parameters a, b, c, and d characterize the T_1 quadratic map. The T_0 map has at the origin unstable and stable eigenvalues λ_u, λ_s, respectively. In the following, we assume for simplicity that these eigenvalues are independent of the parameter μ. Recall that for a map, unstable and stable eigenvalues are such that $|\lambda_s| < 1 < |\lambda_u|$. Moreover, we suppose $|\lambda_u| < 1/|\lambda_s|$, which implies the saddle orbit to be dissipative. Since the flows are orientation preserving in 3D, we have either $\lambda_u, \lambda_s < 0$ or $\lambda_u, \lambda_s > 0$.

The number n of times that T_0 has to be applied coincides with the numbers of turns that the flow performs around the saddle cycle before escaping along the reinjection path. The existence of an infinite set of periodic orbits accumulating at $\mu = 0$ and their bifurcations have been studied by Gavrilov and Sil'nikov using the maps $T_1 \circ T_0^n$ defined as a combination of the above maps:

$$T_1 \circ T_0^n(x,y) = (\lambda_s^n [x_H + a(y - y_H)], \lambda_u^n [b\mu + cx + d(y - y_H)^2/2]) \ . \tag{3}$$

It has also been proven by the same authors that, at $\mu = 0$ and for all $n > k$, where integer k depends on system parameters, each map $T_1 \circ T_0^n$ has a horseshoe. Depending on the signs of the parameters $c, d, \lambda_s, \lambda_u$, different geometrical configurations of the manifolds arise. The one we are dealing with in the following, observed experimentally in LSA, is obtained when $c, d, \lambda_s, \lambda_u > 0$. Then for $\mu \to 0$, with stable and unstable manifolds of the saddle cycle approaching each other without having their first intersection, periodic solutions, which are fixed points of $T_1 \circ T_0^n$ at increasing high n values, are generated through saddle-node bifurcations. Each of these fixed points undergoes a period-doubling cascade of bifurcations which, for some n values, leads to formation of a horseshoe for the $T_1 \circ T_0^n$ map. In the limit of infinite dissipation $\lambda_s^n \to 0$, maps of Eq. (3) may be written as 1D maps

$$T_1 \circ T_0^n(x,y) \to f_\mu^n(y) = \lambda_u^n [b\mu + d(y - y_H)^2/2] + O(\lambda_u^n \lambda_s^n) \ . \tag{4}$$

The analysis to be developed here may be applied also to the maps $T_0^n \circ T_1$, defined as

$$T_0^n \circ T_1(x,y) = (x_H - a(\lambda_u^n y - y_H), b\mu + \lambda_s^n x + \tfrac{1}{2} d(\lambda_u^n y - y_H)^2) \ . \tag{5}$$

In the limit $\lambda_s^n \to 0$ the dependence on x disappears and we have study the following 1D maps:

$$T_0^n \circ T_1(x,y) \to g_\mu^n(y) = b\mu + \tfrac{1}{2} d(\lambda_u^n y - y_H)^2 + O(\lambda_u^n \lambda_s^n) \ . \tag{6}$$

If we multiply Eq. (6) by λ_u^n and use the renormalized variable $\lambda_u^n y$ instead of y, we get exactly the same maps of Eq. (4), so that the same bifurcation sequence is obtained. The bifurcations are the same as in the 2D case. Decreasing the μ parameter, first f_μ^n approaches the first quadrant diagonal where a couple of fixed points of f_μ^n, stable and unstable, are created through tangent bifurcations. Then the stable fixed points undergoes a period-doubling cascade eventually leading to chaos, while f_μ^{n+1} approaches the tangent bifurcation, which is equivalent to that reached in type-I intermittency.

Two different situations arise depending on a condition, to be derived in the following subsections, on the d parameter, which is related to the reinjection process. In one case, for an interval of the control parameter μ where neither f_μ^n or f_μ^{n+1} have stable fixed points, the full maps of Eqs. (4) and (6) are explored by the system. The main difference between the two maps is that the one of Eq. (4) gives parabolas with the vertex aligned on the vertical line $y = y_H$, while that of Eq. (6) gives parabolas with vertex aligned on the horizontal line at coordinate $b\mu$. For Eq. (4) the vertex position scales as $\lambda_u^n b\mu$ and vertical separation between different parabolas increases increasing the number n. For Eq. (6) the vertex position scales as $\lambda_u^{-n} y_H$ and horizontal separation between different parabolas decreases increasing the number n. This behavior is represented in Fig. 5 where the theoretical maps f_μ^n and g_μ^n are plotted for the same values of control parameters. This overall behavior is based on the simultaneous presence of period-doubling bifurcations for f_μ^n and a tangent bifurcation for f_μ^{n+1}. Notice that the presence of multibranched maps is evidence of this specific chaotic behavior. An important result derived from the above analysis is that the branches are denoted by the number n of turns that the flow performs around the saddle cycle before escaping along the reinjection path.

In the other case, for different values of the d parameter, intervals of bistability between stable fixed points of f_μ^n and f_μ^{n+1} are present. In this situation it is almost impossible to observe branched maps, period-doubling cascade, and chaotic behavior. A small amount of noise unavoidable in the experiments, induces switches among the coexisting stable solutions and the map shows points distributed on a lattice, each point corresponding to a particular transition $f_\mu^n \to f_\mu^m$ between a couple of solutions. In the experiments, we have observed branched maps using CH_3I as the intracavity absorber, and maps with a lattice structure using SF_6. The laser intensity versus time signal was surprisingly similar in the two cases, because we have in both cases an unstable saddle

cycle with very similar geometry of the stable and unstable manifolds. We wish to point out here that our simplified model explains both the experimentally observed behaviors, even if we need to introduce a small amount of noise in order to explain the lattice.

The limit $\lambda_s^n \to 0$, studied here, can be obtained either with $\lambda_s \to 0$ or with $n \to \infty$. The first case refers to systems with infinite dissipation, while the second case refers to orbits of arbitrary high periodicity in systems whose dissipation may be low. It should be noticed that most experiments concerned with homoclinic orbits are performed in strongly dissipative systems, so that the $\lambda_s \to 0$ limit applies for comparison with experiments. On the contrary, orbits of very high periodicity (the limit $n \to \infty$) are unlikely to be detected experimentally, because their attraction basins are very small and the experimental noise masks all high-frequency components. A case of infinite dissipation was studied by Gaspard and Wang [10], who considered the limiting case of T_1 maps infinitely contractive to a single point of Π_0, independently of the initial condition in Π_1. The different case studied here shows results similar to that investigated by Argoul, Arneodo, and Richetti [19] for a saddle focus. Roughly speaking, in our case the region of infinite dissipation is a neighborhood of the saddle cycle, while in the Gaspard and Wang case the infinite dissipation comes from the reinjection process, i.e., from a region around the homoclinic path, far from the saddle.

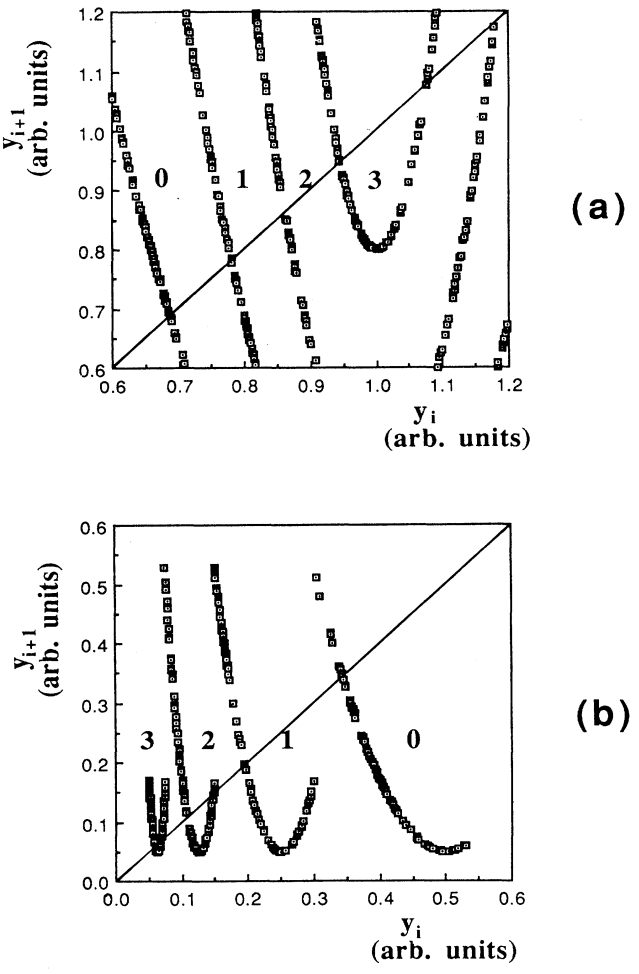

FIG. 5. In (a), return maps $y_{i+1}=f_\mu^n(y_i)$; and in (b), return maps $y_{i+1}=g_\mu^n(y_i)$ for the following control parameter values: $b=1$, $d=6$, $\lambda_u=2$, $\mu=0.05$, $\epsilon_1=0.4$, $\lambda_u^{-1}(1+\epsilon_2)=1-\epsilon_1$. The 400 point maps shown in each case correspond to random initial conditions.

B. Branch limits

In this subsection we define more precisely the maps introduced in the preceding subsection. Depending on the geometry of stable and unstable manifolds, different situations may arise, but the most interesting ones for applications are shown in Fig. 6. The intersection between the S plane and L orbit is point O represented in Figs. 6(a) and 6(b), together with the stable and unstable manifolds on the plane S. Around point O there is a region of the plane S where linearization of the flow of Eqs. (1) holds. Inside this region, there is a Π_1 neighborhood of the point $M^-=(0,y_H)$ which lies on the unstable manifold W^u. Due to the geometry of the unstable manifold

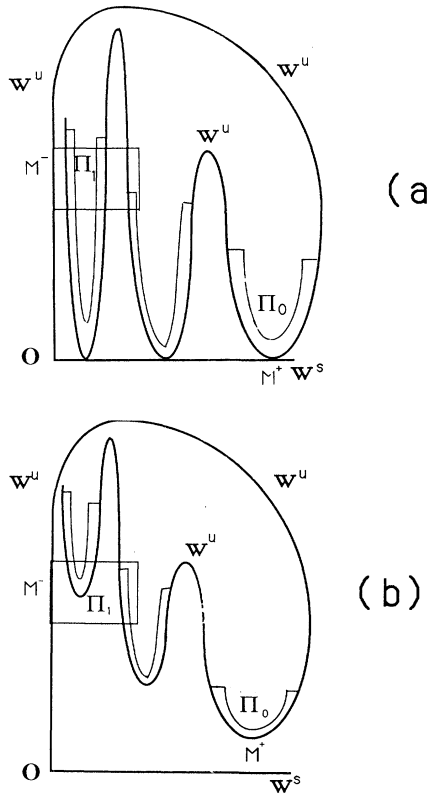

FIG. 6. Sketch of stable W^s and unstable W^u manifolds, set Π_0 around point M^+ and set Π_1 around point M^- on the section plane S for $c,d,\lambda_s,\lambda_u>0$ and (a) $\mu=0$, (b) $\mu>0$. The images of set Π_0 by application of T_0 are also sketched.

W^u, the flow reinjects points of Π_1 inside the linearization region, into a Π_0 neighborhood of the point $M^+=(x_H,b\mu)$ which is the image of M^- and lies on the unstable manifold W^u. The point M^+ is the point of Π_0 with minimum vertical coordinate. Once in the Π_0 region, the flow moves back towards region Π_1. The positions of M^- and M^+ points change with the μ parameter and when $\mu=0$ these points, with coordinates $M^-=(0,y_H)$, $M^+=(x_H,0)$, are the intersections between the homoclinic curve Γ and the section plane S. We have schematically represented all these regions in Figs. 6(a) and 6(b), respectively, for the cases $\mu=0$, where the homoclinic orbit to the saddle cycle exists, and $\mu>0$, where that homoclinic orbit does not exist. Notice that, in the latter case, also in the absence of the homoclinic orbit, the reinjection process is provided by the shape of the manifolds.

The domain of the T_0 map is the region of linearization on the plane S. T_0 is used to mimic the motion between Π_0 and Π_1. The domain of the T_1 map is the Π_1 neighborhood of the point M^- and its image is the Π_0 neighborhood of the point M^+. The compositions of these maps are defined as $T_1\circ T_0^n$: $\Pi_1\rightarrow\Pi_1$ and $T_0^n\circ T_1$: $\Pi_0\rightarrow\Pi_0$, respectively. T_1 is used to mimic the motion between Π_1 and Π_0, and it has a quadratic form given by the geometry of the unstable manifolds. Following images of Π_0 under application of T_0 and T_1 maps, it is straightforward to realize that, in order to describe without ambiguity the evolution of each point with iterations of these maps, the following conditions must be satisfied:

$$T_0\Pi_0\cap\Pi_0=0\ , \tag{7a}$$

$$T_0^{-1}\Pi_1\cap\Pi_1=0\ . \tag{7b}$$

Without losing generality, we shall put $y_H=1$ in the following. In the case where subsets Π_1^n of Π_1 exist such that

$$\Pi_1\supset f_\mu^n(\Pi_1^n) \tag{8}$$

at least for some μ and n values and for a set of initial conditions, the system remains confined in regions around the stable and unstable manifolds, where the approximate 1D quadratic maps of Eq. (5) reproduce by iteration the overall dynamics. Set Π_1 is defined as

$$\Pi_1=(1-\epsilon_1,1+\epsilon_2)\ , \tag{9a}$$

where $\epsilon_1,\epsilon_2>0$ are supposed to be independent of μ for sake of simplicity. The origin of the Π_1 asymmetry with respect to the point $y_H=1$ is better understood in 2D. In effect the horseshoe-shaped region $T_0^n(\Pi_0)$ of Fig. 6(b) may be only partially mapped into Π_1. Moreover, the x extension of the Π_1 region, which we draw constant in Fig. 6 for simplicity, may be larger near the stable manifold, where the system is strongly pushed towards the saddle cycle and the unstable manifold. In this case, the part of the left vertical strip of region $T_0^n(\Pi_0)$ mapped into Π_1 is smaller than the part of the right vertical strip of region $T_0^n(\Pi_0)$ mapped into Π_1. Even if Π_1 asymmetric intervals may not allow formation of a horseshoe for the $T_0^n\circ T_1$ maps, those intervals are still very useful to understand the effect on the overall dynamics of the stable and unstable manifolds.

The constraint of Eq. (7b) imposes that the Π_1 extension satisfies the following condition:

$$\lambda_u^{-1}(1+\epsilon_2)\leq 1-\epsilon_1\ . \tag{9b}$$

When an equality holds, Π_1 has the largest allowed amplitude. Using Eqs. (5), (8), and (9a) we deduce the following relation defining the y extension of the Π_1^n subsets:

$$1-\epsilon_1\leq\lambda_u^n[b\mu+d(y-1)^2/2]<1+\epsilon_2\ . \tag{10}$$

In the multibranched maps of Fig. 5, observed at a given value of the μ parameter, there are as many branches as there are intervals Π_1^n satisfying Eq. (10). The full extension of the branches is observable only in chaotic regimes, while only few points are observed in periodic regimes. However, the different periodic solutions, their stability windows, and their bifurcations depend on the global structure of the branches.

From Eq. (10) we find that, for the case $\mu>0$, if f_μ^n contains a subset Π_1^n, the control parameter μ satisfies the following condition:

$$\sup\{0,[\lambda_u^{-n}(1-\epsilon_1)-d\ \sup\{\epsilon_1,\epsilon_2\}^2/2]/b\}<\mu<\lambda_u^{-n}(1+\epsilon_2)/b\ . \tag{11}$$

It is straightforward to derive from Eqs. (9b) and (10) that there are no overlaps between Π_1^n and Π_1^{n+1}. When Π_1 has the largest amplitude, and equality holds in Eq. (9b) and there are no gaps between the extensions of subsets Π_1^n and Π_1^{n+1}. In other cases, the presence of gaps implies that, for some initial conditions inside Π_1, the orbit escapes from Π_1.

The fixed points of f_μ^n are found imposing

$$y=\lambda_u^n[b\mu+d(y-1)^2/2] \tag{12a}$$

a second-order equation with solutions $y_\pm^n$. By introducing $\zeta=y-1$ we may write the fixed-point positions as

$$\zeta_\pm^n=\lambda_u^{-n}/d\pm[\lambda_u^{-2n}/d^2-2(b\mu-\lambda_u^{-n})/d]^{1/2}\ . \tag{12b}$$

By imposing the term under the square root to be positive, it results that real fixed points exist only when

$$\mu\leq\lambda_u^{-n}(1+\lambda_u^{-n}/2d)/b\ . \tag{13}$$

When an equality holds in Eq. (13), the two fixed-point solutions $\zeta_\pm^n$ coalesce. In Fig. 5 these fixed points are the intersections between the maps and the diagonal of the first quadrant.

C. Stability, bistability, and instability

The 1D maps of Eq. (5) are real and may lose stability only by tangent or flip bifurcations. This statement is valid not only in the case of infinite dissipation, but also in the 2D case when the area contraction of $T_1\circ T_0^n$ near point O dominates any expansion elsewhere and a one-dimensional center manifold is obtained. Under these hy-

potheses the instability is associated with the passage of simple eigenvalues of the Jacobian matrix of the map $T_1 \circ T_0^n$ through ± 1 [18]. The stability condition becomes in our case

$$-1 \leq f'^n_\mu = \lambda_u^n d\xi \leq 1 \ . \tag{14a}$$

When Eq. (14a) is applied to the ξ^n_+ solution, it is straightforward to demonstrate that that solution is always unstable. At the ξ^n_- solution we have

$$-2\lambda_u^{-n}/d \leq -[\lambda_u^{-2n}/d^2 - 2(b\mu - \lambda_u^{-n})/d]^{1/2} \leq 0 \ . \tag{14b}$$

The right-hand side (rhs) condition is always satisfied when ξ^n exists. The left-hand side (lhs) is satisfied when

$$\mu \geq \lambda_u^{-n}(1 - 3\lambda_u^{-n}/2d)/b \ . \tag{15}$$

From (12b) and (15) we deduce that ξ^n_- exist and is stable whenever

$$\lambda_u^{-n}(1 - 3\lambda_u^{-n}/2d)/b \leq \mu \leq \lambda_u^{-n}(1 + \lambda_u^{-n}/2d)/b \ . \tag{16}$$

The width $\Delta\mu_s^n$ of the stability region associated with the Π_1^n subset is given by

$$\Delta\mu_s^n = 2\lambda_u^{-2n}/bd \ , \tag{17}$$

which represents the leading term of the stability window in the 2D case [10]. For the limits of the stability region, we notice that at the lower limit, associated with the -1 eigenvalue, the stability is lost through a flip or period-doubling bifurcation. At the upper limit, associated with the 1 eigenvalue, stability is lost through a tangent bifurcation.

By applying Eq. (16) to f_μ^n and f_μ^{n+1} maps, we find that if the following condition is fulfilled:

$$\lambda_u^{-(n+1)}(1 + \lambda_u^{-(n+1)}/2d)/b < \mu < \lambda_u^{-n}(1 - 3\lambda_u^{-n}/2d)/b \ , \tag{18}$$

we have an interval of μ values where neither f_μ^n nor f_μ^{n+1} have stable fixed points. The condition of Eq. (18) does not imply the presence of a horseshoe, but, if it is fulfilled, a complicated behavior between the fixed points of f_μ^n and f_μ^{n+1} is observed. From Eq. (18) we derive a condition on the parameter d

$$d > \lambda_u^{-n}(\lambda_u^{-2} + 3)/[2(1 - \lambda_u^{-1})] \ . \tag{19}$$

In between the stability intervals, we obtain the μ value instability interval which is an interval of width $\Delta\mu_{\text{in}}^n$

$$\Delta\mu_{\text{in}}^n = \lambda_u^{-n}/b(1 - \lambda_u^{-1}) + O(\lambda_u^{-2n}) \ , \tag{20}$$

where f_μ^n undergoes a sequence of period-doubling bifurcations eventually leading to chaos and f_μ^{n+1} approaches the tangent bifurcation, giving rise to ξ^n_+ and ξ^n_-. Intervals $\Delta\mu_s^n$ and $\Delta\mu_{\text{in}}^n$ are shown in Fig. 7(a) for different n values and for the same control parameters of Fig. 5. If condition (19) is not fulfilled, intervals of bistability between stable fixed points of f_μ^n and f_μ^{n+1} are present, as is shown in Fig. 7(b).

The d parameter of the T_1 map has an important role in the occurrence of complicated dynamics in our system.

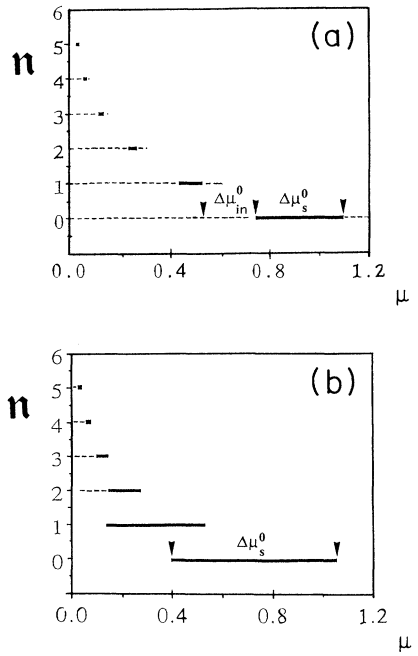

FIG. 7. Parameter μ intervals for existence, stability, and instability of the $f_\mu^n(y)$ map with n from 0 to 5. In (a), same control parameters as in Fig. 5; in (b), $\lambda_u = 2$, $b = d = 1$, $\epsilon_1 = 0.48$, $\lambda_u^{-1}(1 + \epsilon_2) = 1 - \epsilon_1$. Thick horizontal segments define the regions $\Delta\mu_s^n$ of fixed point stability; the dashed lines denote the parameter μ instability intervals. The $\Delta\mu_{\text{in}}^n$ intervals are defined as the regions in between stability regions of f_μ^n and f_μ^{n+1}. In (a), for each n value, stability is lost on the right side through a tangent bifurcation, and on the left side through period-doubling bifurcation. In (b), tangent bifurcations are observable only for f_μ^n with $n \geq 4$ while period-doubling bifurcations are observable only for f_μ^n with $n \geq 2$.

At a given λ_u, Eq. (19), the condition for chaotic behavior, imposes a relation between the n and d values. An increase in d corresponds to a decrease in the n value where it is possible to have a region of instability between fixed points of f_μ^n and f_μ^{n+1}. Equation (20), a scaling law for the chaotic windows, leads to larger windows at low n values, i.e., windows which are more easily detected experimentally. Furthermore, the d parameter controls the expansion of the map in the region along the reinjection path. In effect in the 1D limit we have

$$T_1(x,y) \to f_{1\mu}(y) = b\mu + \tfrac{1}{2}d(y-1)^2 \ . \tag{21}$$

The expansion or contraction rate of $f_{1\mu}(y)$ is given by

$$|f'_{1\mu}(y)| = d|y - 1| \tag{22}$$

and it is independent of the parameter μ. A large d value leads to very wide structures in phase space, easy to detect experimentally on the recorded variable and to analyze for chaotic behavior. In conclusion, all the requirements for the occurrence and detection of complicated dynamics are enhanced by increasing the d parameter.

IV. HOW TO USE THE TIME RETURN MAPS IN ALMOST 1D SYSTEMS

The return time maps have been introduced by Arecchi *et al.* [2] for the study of an experimental system whose instability was explained in terms of homoclinic orbit associated with a saddle focus. The theoretical map was in that case derived under the approximation that the system spends most of the time near the saddle focus. Here we study systems where this approximation is no longer valid. The aim of our work is to find some reasonable hypotheses under which it is possible, starting from maps of Eqs. (4) or (6), to derive analogous maps for the time of flight or return time. Although these hypotheses are not generic, they appear to apply to a large number of physical systems. In these systems, as clearly shown for the LSA data in Sec. II, the time return maps give the same information as the maps described previously, but with the enormous advantage that these maps are much easier to be extracted from experimental data.

The time of flight between two planes S_1 and S_2 is a function of the initial condition x_1 on the starting plane S_1. More precisely, the time of flight T^{S_1,S_2} is the line integral of the reciprocal of the velocity $\mathbf{G}_\mu(\mathbf{x})$ along the trajectory from plane S_1 to plane S_2, as denoted in Fig. 1:

$$T^{S_1,S_2}=F_\mu(\mathbf{x})=\int_{\mathbf{x}_1}^{\mathbf{x}_2} d\mathbf{X}(\mathbf{x}_1)\frac{\mathbf{G}_\mu(\mathbf{X}(\mathbf{x}_1))}{|\mathbf{G}_\mu(\mathbf{X}(\mathbf{x}_1))|^2}\ , \tag{23}$$

where $\mathbf{X}(\mathbf{x}_1)$ is the orbit solution of Eq. (1) with initial conditions $\mathbf{x}_1$. The point $\mathbf{x}_2$ is the first intersection of the orbit $\mathbf{X}(\mathbf{x}_1)$ with the plane S_2 and depends on $\mathbf{x}_1$. Thus the time of flight between planes S_1 and S_2 is a function of the initial condition $\mathbf{x}_1$ on the starting plane S_1. We may introduce also the return time $T^{\text{ret}}=T^{S_1,S_1}$ as the time of flight from plane S_1 back to the same plane.

Let us comment on the continuity of Eq. (23). In general, if we choose the section planes such that no tangent intersections exist, because as long as $\mathbf{G}_\mu(\mathbf{x})\neq 0$, the inverse of the velocity has the same regularity of the equation $\mathbf{G}_\mu(\mathbf{x})$, a discontinuity may arise only from the length of the path between the section planes. In our system, see Fig. 1, the function $F_\mu(\mathbf{x})$ has a discontinuity if, between the starting and arrival planes, orbits turn a different number of times around the saddle cycle. This is the case when we measure the total time between two consecutive laser pulses. Geometrically, this means that the flow associated with the orbits and originated by points on the starting plane is broken into different parts, each one with its own trajectory. The function $F_\mu(\mathbf{x})$ has discontinuities also if, before the arrival plane drawn in Fig. 1, the different parts of the flow are merged. This discontinuous behavior may be understood as a type of memory effect due to the integral form of the Eq. (23). Between planes S_1 and S_2 shown in Fig. 1, there are no discontinuities in the function $F_\mu(\mathbf{x})$. This choice of the planes S_1 and S_2 corresponds to the measure of time between the end of one laser pulse and the beginning of the next. On the contrary, by choosing S_2 as the starting plane and S_1 as the arrival plane of Fig. 1, discontinuities in the time of flight appear. This choice of the planes S_1 and S_2 corresponds to measuring the full duration time of the laser pulses. Moreover, in the first case, the time of flight is finite also along the homoclinic orbit, while, in the second case, the time of flight along the homoclinic orbit is infinite.

The function F_μ depends on the choice of the section planes and under a suitable chose it may provide an amplification of the sensitivity. For instance, if the section planes are placed in regions where the flow may be linearized around some equilibrium solution, as the saddle focus of Ref. [2], or the saddle cycle, this amplification is exponential. This amplification may be verified taking only the first-order terms in x and y in Eqs. (1b). Similar equations holds for the saddle focus case.

If the system is almost undimensional, the points on the Poincaré section planes lie on a undimensional manifold which is parametrized by the variable z, as it applies for instance to the LSA data analyzed in Sec. II. In this case the time of flight or the return time are functions whose only variable is z. If $F_\mu(z)$ is continuous, it is invertible in each interval between two local maximum and minimum. Let us introduce now the index i to denote the number of iterations of the global map, which corresponds to the number of reinjections into the neighborhood of the saddle cycle. Furthermore, n_i is the number of turns around the saddle cycle performed by the flow after the ith reinjection, before escaping from the saddle-cycle region and coincides with the number of times the T_0 map has to be applied before reinjection. If T_i denotes either the time of flight or the return time corresponding to the ith reinjection we may write

$$T_i=F_\mu(f_\mu^{n_i-1}(F_\mu^{-1}(T_{i-1})))\ , \tag{24}$$

where F_μ^{-1} is the inverse function of F_μ. When F_μ is monotonic, it has only one inverse function defined on all the domain of F_μ and then Eq. (24) has exactly the same number of branches and the same number of critical points of Eq. (4). Thus we may code the dynamics of the system studying Eq. (24) as well as Eq. (4), i.e., from the point of view of symbolic dynamics, Eq. (4) and Eq. (24) provide the same information. As standard in the symbolic dynamics of undimensional maps [22], the number of symbols is given by the sum of the number of semibranches with positive slope plus the number of semibranches with negative slope plus the number of critical points. When F_μ is not monotonic, F_μ^{-1} is multivalued as is also Eq. (24), with different branches having a common point that is the image, under Eq. (24), of a local maximum or minimum. This happens, for instance, if there are particular symmetries in both $\mathbf{G}_\mu(\mathbf{x})$ and the starting and arrival planes. In this case we cannot derive the symbolic dynamics of the system from Eq. (24), but the return time map is still very convenient to detect a multibranched structure in f_μ^n. Let us notice that by defining the planes S_1 and S_2 as planes with constant laser intensity, it is possible to derive 1D maps avoiding the phase-space reconstruction.

V. MAP COMPARISON

When the maps of Fig. 3(a) derived from the LSA experimental results are compared to those of Fig. 5(b), derived from the theoretical 1D maps of Eq. (7), a very striking similarity becomes apparent. This similarity between LSA and 1D maps becomes more complete if the transformation $y \rightarrow -y$ is applied to Eq. (6). This transformation is equivalent to a reparametrization of the unidimensional manifold on the Poincaré plane. The similarity of these maps confirms the result of a LSA chaos as being associated with the presence of a tangency of homoclinic bifurcation in a system with a reinjection to a saddle cycle.

Laser intensity maps similar to those of Fig. 3(a) have been obtained for all the CH_3I data we have analyzed through phase-space reconstructions and Poincaré sections. If the used Poincaré section crosses orbits that leave or enter the phase-space region where the saddle cycle is contained, the experimental map is to be compared with Eq. (4) or Eq. (6), respectively. Actually, the possibility of observing these two different maps depends on the separation between the orbits, or more precisely on the expansion or contraction of the flow. This orbit separation is in some regions of phase space greater than in others and it is not always possible to compare the experimental results with both Eqs. (4) and (6).

Considering the discussion of the function $F_\mu(z)$ introduced in Sec. IV for the time of flight, the equivalence of the intensity and time-of-flight maps of Fig. 3 confirms that for those experimental observations the function $F_\mu(z)$ is continuous, and moreover is invertible. We deduce also that the laser flow is confined in one region of phase space.

The results of Fig. 3(b) may be reproduced supposing a linear relation for the z dependence of the time of flight. Let us suppose we have a point z^* such that

$$F'_\mu(z^*)=\alpha \neq 0 \ . \tag{25}$$

For points z near to z^* we may write

$$T_i=F_\mu(z_i)\approx F_\mu(z^*)+\alpha(z_i-z^*)=T^*+\alpha(z_i-z^*) \ , \tag{26}$$

where T^* is the time of flight corresponding to the coordinate z^*. Making use of this relation between z_i and T_i, and applying the 1D maps of Eq. (4) to the z_i variable, we obtain

$$T_i=T^*-\alpha z^*+\alpha\{f_\mu^{n_i-1}[z^*+(T_{i-1}-T^*)/\alpha]\} \ . \tag{27}$$

This functional relation between the times of flight of the iteration has the same dependence as that of the 1D map for the z coordinate as presented in Eq. (4). Thus, for a linear relation between the time and the z coordinate, the two experimental maps of Fig. 3 have the same shape.

For the experimental results of Figs. 4(a) and 4(b) where maps of T^{ret} return times and T^{S_1,S_2} times of flight are reported, we observe three different branches, corresponding to $n=0,1,2$. The return time return maps are composed of a greater number of branches than in the case of the time of flight, because the function $F_\mu(z)$, relating time to the z coordinate, has some discontinuities. Again a linear approximation allows us to reproduce the experimental results. If the time needed by the system to turn n times around the saddle cycle is approximated as nT_C, with T_C the period of the saddle cycle, we have

$$\begin{aligned} T_i^{\text{ret}} &= n_i T_C + T^* + T_i \\ &\approx n_i T_C + T^* + \alpha f_\mu^n(z^* + (T_{i-1}^{\text{ret}} - \tau^* - n_{i-1} T_C)/\alpha) \ . \end{aligned} \tag{28}$$

The number of functions f_μ^n with a different n involved in this equation is the same as in Eq. (27), but now each branch corresponding to one f_μ^n is split into as many branches as there are different possible n_{i-1} in the preimage of f_μ^n. Recall that n_i has been defined as the number of turns around the saddle cycle performed by the system after the ith reinjection. A clear evidence of this property is shown in Figs. 4(d) and 4(c) where we have plotted the maps corresponding, respectively, to the return time of Eq. (28) and to the time of flight of Eq. (27). In Fig. 4(c), as well as the experimental map of Fig. 4(a), we observe three different branches, corresponding to $n=0,1,2$. Moreover, in Figs. 4(b) and 4(d), experiment and theory for T^{ret}, respectively, we notice that no branches appear in the lower right-hand corner. The missing branch corresponds to the sequence $n=0 \rightarrow n=2$, which is forbidden for this value of the control parameter. In principle, this selection rule could have been deduced also by the shape and the extension of the branches of Figs. 4(a) and 4(c). The utility of the return time return map is that selection rules on the sequence of laser pulses with different n are immediately detected.

Comparison between theory and experiment of Figs. 3–5 shows that the simple model presented here is able to reproduce qualitatively the relative position, the shape of the branches according to the number n, and also the selection rules. In both Figs. 3 and 4 we have no evidence of the appearance, for the same n value, of a second branch with positive slope, as happens in the theoretical maps of Fig. 5. This behavior happens for two different reasons. The first reason is connected to the already mentioned asymmetry in the interval Π_1. Points with $y < y_H$ give rise to branches with negative slope, and points with $y > y_H$ give rise to branches with positive slope. Thus branches with positive slope are very difficult to observe in the case where the position of the point y_H is very near to the superior extreme of the allowed interval Π_1. The second reason is related to the procedure used to derive the experimental maps. The points are reinjected in the section plane on a line which is folded, as is shown in Fig. 5. In a strongly dissipative system it is very difficult to resolve the folding of the manifold and for this reason the two branches overlap in the intensity map. Looking to the time map, we notice that the map of our model has an inversion symmetry at the point y_H due to the quadratic term. If this symmetry is present also in the function $\mathbf{G}_\mu(\mathbf{x})$, then, as we mentioned before, F_μ^{-1} is multivalued and the two branches cannot be resolved. Fortunately, a small correction of odd order

violates the symmetry and the two branches may be resolved. This happens in some experimental data and also in the numerical simulation of Ref. [15], where the two branches appear on the same side with a small separation.

As final remark, let us point out that in our experiment we had observed chaotic signals with values of n ranging from 0 to 4. Looking at the lower bound of Eq. (18), for $\lambda_u > 1$ and this low n value, the lower bound of the μ parameter results in a value much larger than 0, corresponding to the homoclinic tangency.

VI. CONCLUSION

The most important results obtained with a simple model of a quadratic homoclinic tangency associated with a saddle cycle are the existence of branched structure in the return maps of flight, the return time and the return intensity. Each of these branches corresponds to laser pulses with the same number n of oscillation around the saddle cycle. We have also found that, depending on the choice of the starting and arrival planes, we may define different time-of-flight return maps. Some of them are equivalent to the intensity return maps because they are equivalent in the codification of the dynamics. All these 1D maps are very useful in pointing out a chaotic behavior associated with a particular configuration of the stable and unstable manifolds of a saddle cycle. Chaotic behavior is experimentally observed when these manifolds are approaching each other, even in a region of control parameters far from the homoclinic tangency, where the homoclinic orbit still does not exist.

The quadratic tangency is an approximation valid only in a small neighborhood of the point y_H. A more precise model of the experiment requires the introduction of higher-order terms both in the modeling of the reinjection process and in the modeling of the escape from the saddle cycle. These corrections will not affect, in the 1D limit, the order of the sequence of the bifurcations leading to the complicated dynamics observed, but they will modify only the extension of their stability regions. For instance, let us consider the map used by Pikovsky [14] to reproduce the BZ reaction, maps composed of a linear part, modeling the escape from an unstable periodic solution, and by a nonlinear part, not simply quadratic, modeling the reinjection process. The sequence of bifurcations and the shape of the solutions both in those experiments and model is surprisingly similar to those presented in our model and observed in LSA. Note that the rich phenomenology observed in both LSA and BZ cannot be described only with this model. In other situations the shape of the LSA experimental signal is no longer composed of a mixture of pulses with large and small peaks. In particular, we have not described here the bifurcations leading to the saddle-cycle creation. However, we have some preliminary indication that the geometrical organization of LSA phase space remains the same. Finally we want to mention that we have observed both in the numerical simulation and in the LSA experiment periodic orbits that are compositions of some simple periodic orbits as described prior. These orbits have been theoretically predicted in the case of quadratic tangent bifurcation by Gavrilov and Sil'nikov [8,9] and have been numerically observed also by Pilovsky [14]. These orbits give important information about the topological organization of the flow and are the subject of current investigation.

ACKNOWLEDGMENTS

The authors would like to thank B. Zambon for useful discussions. One of us (F.P.) also wishes to thank U. Bessi, P. Mayer, and H. G. Solari.

[1] J. C. Roux and H. L. Swinney, in *Nonequilibrium Dynamics in Chemical Systems,* edited by C. Vidal and A. Pacault (Springer, Berlin, 1984), p. 124; J. C. Roux and A. Rossi, in *ibid.*, p. 141.

[2] F. T. Arecchi, A. Lapucci, R. Meucci, H. Mancini, J. A. Roversi, and P. H. Coullet, Europhys. Lett. **6**, 677 (1988); F. T. Arecchi, W. Gadomski, A. Lapucci, R. Meucci, H. Mancini, and J. A. Roversi, J. Opt. Soc. Am B **5**, 1153 (1988).

[3] J. V. Moloney, J. S. Uppal, and R. G. Harrison, Phys. Rev. Lett. **59**, 2868 (1987); C. O. Weiss, N. B. Abraham, and U. Hubner, *ibid.* **61**, 1587 (1988).

[4] D. Hennequin, F. de Tomasi, B. Zambon, and E. Arimondo, Phys. Rev. A **37**, 2243 (1988).

[5] M. Tachikawa, F. L. Hong, K. Tani, and T. Shimizu, Phys. Rev. Lett. **60**, 2266 (1988); **61**, 1042 (1988).

[6] D. Dangoisse, A. Bekkali, F. Papoff, and P. Glorieux, Europhys. Lett. **6**, 335 (1988).

[7] F. de Tomasi, D. Hennequin, B. Zambon, and E. Arimondo, J. Opt. Soc. Am. B **6**, 45 (1989).

[8] N. K. Gavrilov and L. P. Sil'nikov, Mat. Sb. **17**, 467 (1972).

[9] N. K. Gavrilov and L. P. Sil'nikov, Mat. Sb. **19**, 139 (1973).

[10] P. Gaspard and X. J. Wang, J. Stat. Phys. **48**, 151 (1987).

[11] S. M. Hammel, C. K. R. T. Jones, and J. V. Moloney, J. Opt. Soc. Am. B **2**, 552 (1985).

[12] B. Zambon, Phys. Rev. A **44**, 688 (1991).

[13] R. H. Simoyi, A. Wolf, and H. L. Swinney, Phys. Rev. Lett. **49**, 245 (1982).

[14] A. S. Pikovsky, Phys. Lett. **85A**, 13 (1981).

[15] D. Hennequin, M. Lefranc, A. Bekkali, D. Dangoisse, and P. Glorieux, in *Measures of Complexity and Chaos,* edited by N. B. Abraham, A. M. Albano, A. Passamante, and P. E. Rapp (Plenum, New York, 1990), p. 299.

[16] F. Papoff, A. Fioretti, E. Arimondo, and N. B. Abraham, in *Measures of Complexity and Chaos,* edited by N. B. Abraham, A. M. Albano, A. Passamante, and P. E. Rapp (Plenum, New York, 1990), p. 309.

[17] P. J. Holmes and D. C. Whitley, Philos. Trans. R. Soc. London Ser. A **311**, 43 (1984).

[18] J. Guckenheimer and P. J. Holmes, *Nonlinear Oscillations,*

Dynamical Systems and Bifurcations of Vector Fields (Springer Verlag, New York, 1984).
[19] F. Argoul, A. Arneodo, and P. Richetti, J. Chim. Phys. **84**, 1367 (1987).
[20] A. Fioretti, F. Molesti, F. Papoff, B. Zambon, and E. Arimondo (unpublished).
[21] H. B. Lin, *Elementary Symbolic Dynamics and Chaos in Dissipative Systems* (World Scientific, Singapore, 1989).
[22] L. P. Sil'nikov, Mat. Sb. **3**, 353 (1967).